Physics of the Earth and Planetary Interiors 361 (2025) 107331

Contents lists available at ScienceDirect

Physics of the Earth and Planetary Interiors

journal homepage: www.elsevier.com/locate/pepi

# Effect of chemistry on the compressibility and high-pressure structural evolution of the $CaFe_2O_4$-type aluminous silicate phase

Giacomo Criniti [a,b,*], Tiziana Boffa Ballaran [a], Alexander Kurnosov [a], Takayuki Ishii [c], Elena-Marie Rogmann [a,d], Konstantin Glazyrin [e], Timofey Fedotenko [e], Daniel J. Frost [a]

[a] Bayerisches Geoinstitut, University of Bayreuth, Bayreuth, Germany
[b] Earth and Planets Laboratory, Carnegie Institution for Science, Washington, DC, USA
[c] Institute for Planetary Materials, Okayama University, Misasa, Japan
[d] School of Earth Sciences, University of Bristol, Wills Memorial Building, Queens Road, Bristol BS8 1RJ, United Kingdom
[e] Deutsches Elektronen-Synchrotron DESY, Notkestr. 85, 22603 Hamburg, Germany

ARTICLE INFO

*Keywords:*
$CaFe_2O_4$-type phase
Lower mantle
Equations of state
Structural refinements
Crystal chemistry
$Fe^{3+}$ spin-crossover

ABSTRACT

Approximately 22–26 vol% of a basaltic phase assemblage at lower mantle conditions is comprised of a (Na,Mg,$Fe^{2+}$)(Al,Si,$Fe^{3+}$)$_2O_4$ phase with $CaFe_2O_4$-type (CF-type) structure. Previous experimental studies attempted to determine the equation of state of the CF-type phase but reported contrasting compressibility values, even for samples with the same composition. Therefore, the elastic properties of the CF-type phase remain, to date, largely unconstrained. Here, we conducted single-crystal X-ray diffraction (SCXRD) measurements in the diamond anvil cell (DAC) at high pressure and room temperature on three samples of CF-type phase with compositions $Na_{0.90(1)}Al_{1.03(2)}Si_{1.00(2)}O_4$ (NaCF), $Na_{0.66(4)}Mg_{0.28(4)}Al_{1.22(3)}Si_{0.78(3)}O_4$ (MgCF) and $Na_{0.62(2)}Mg_{0.19(1)}Fe^{2+}_{0.17(1)}Fe^{3+}_{0.080(4)}Al_{1.20(3)}Si_{0.70(1)}O_4$ (FeCF). A multi-sample loading approach was employed for most DAC runs, where two samples were loaded in the same sample chamber to reduce possible systematic deviations between datasets, thus enhancing internal consistency and corroborating data reproducibility. Experiments on the NaCF and MgCF samples were conducted up to ~50 GPa, while the FeCF sample was compressed to ~72 GPa to better characterize the effect of the spin crossover of octahedrally coordinated $Fe^{3+}$. We found the isothermal bulk modulus ($K_{T0}$) to increase with decreasing $NaAlSiO_4$ content, accompanied by only a slight decrease in its pressure derivative ($K'_{T0}$). Analysis of the crystal structures of the three samples at high pressure allowed compositional trends to be determined also for the interatomic bonds and polyhedral compressibility, as well as the distortion indices. These suggest an overall stiffening of the A site with increasing $Mg^{2+}$ and $Fe^{2+}$ content, as well of the two B sites with increasing $Al^{3+}$ and $Fe^{3+}$ content. Enhanced compressibility of the unit cell and octahedral B sites was observed between ~26–42 GPa in the FeCF sample, suggesting a pressure-induced spin crossover of $Fe^{3+}$, in agreement with some previous observations. Finally, trends in the elastic properties from experimental studies conducted along the $NaAlSiO_4$-$MgAl_2O_4$ join are discussed and used as a proxy to evaluate the reliability of end-member properties for the CF-type phase employed in most recent mineral physical and thermodynamic databases. Our analysis suggests current mineral physical models might underestimate densities and overestimate bulk sound velocities of $NaAlSiO_4$-rich CF-type phases with basaltic composition.

## 1. Introduction

The orthorhombic $CaFe_2O_4$-structured (CF) aluminous phase is one of the main constituents of a subducted oceanic crust phase assemblage at pressures and temperatures of the Earth's lower mantle (e.g., Ono et al., 2001). Its crystal structure (space group: *Pbnm*, Supplementary Material 1, Fig. S1) is comprised of crystallographically distinct, edge- and corner-sharing $B1O_6$ and $B2O_6$ octahedra, occupied mostly by $Al^{3+}$, $Fe^{3+}$ and $Si^{4+}$, and face-sharing $AO_8$ bicapped prisms hosting $Na^+$, $Mg^{2+}$, $Fe^{2+}$ and possibly $Ca^{2+}$ (Akaogi et al., 2024; Ishii et al., 2023; Kojitani et al., 2007; Qin et al., 2023; Yamada et al., 1983). The CF-type crystal structure can thus accommodate almost all major elements constituting a basaltic rock bulk composition, as shown by experimental phase relations studies (Hirose et al., 2005; Hirose and Fei, 2002; Ishii

* Corresponding author at: Bayerisches Geoinstitut, University of Bayreuth, Bayreuth, Germany
*E-mail address:* gcriniti@carnegiescience.edu (G. Criniti).

https://doi.org/10.1016/j.pepi.2025.107331
Received 17 September 2024; Received in revised form 24 December 2024; Accepted 17 February 2025
Available online 19 February 2025

et al., 2022; Ishii et al., 2019; Ono et al., 2001; Ricolleau et al., 2010; Rogmann et al., 2024), as well as in continental crust, terrigenous, and pelagic sediment compositions (Irifune et al., 1994; Ishii et al., 2012). This gives rise to a wide variety of possible charge-coupled chemical substitutions, each described by a specific end-member component, the most relevant being $NaAlSiO_4$, $MgAl_2O_4$, $Fe^{2+}Al_2O_4$, $Fe^{2+}Fe^{3+}_2O_4$, $Mg_2SiO_4$, $MgFe^{3+}_2O_4$, and $CaAl_2O_4$. In addition to these charge-coupled substitutions, the CF-type phase can also host cation vacancies (Ishii et al., 2023; Kojitani et al., 2007; Wang et al., 2023; Wu et al., 2017) which, for compositions relevant to subducted oceanic crust, are argued to be located in the A site based on single-crystal structural analyses (Ishii et al., 2023). As a main constituent of basaltic phase assemblages in the lower mantle, understanding how the structure of the CF-type phase behaves under compression is of particular interest to constrain its stability and elastic properties. As a host of octahedrally coordinated $Fe^{3+}$, the CF-type phase is also likely to undergo a pressure-induced high-to-low spin crossover (Wu et al., 2017), which is known to affect the stability and elasticity of minerals and may be seismically detectable. High concentrations of vacancies could play an important role for noble-gas storage and cycling, and further affect transport properties, such as viscosity, possibly promoting slab delamination in the top-lower mantle (Wang et al., 2023).

Extensive experimental work conducted in the last twenty years was devoted to determining the isothermal equation of state of the CF-type phase, primarily in the $NaAlSiO_4$-$MgAl_2O_4$ system, by means of X-ray diffraction in the diamond anvil cell (DAC) (Dubrovinsky et al., 2002; Guignot and Andrault, 2004; Imada et al., 2012; Qin et al., 2023; Sueda et al., 2009; Wu et al., 2017) and first principle calculations (Kawai and Tsuchiya, 2012; Kawai and Tsuchiya, 2010; Mookherjee, 2011; Wang et al., 2020; Yin et al., 2012). However, the proposed values of isothermal bulk modulus ($K_{T0}$) and its pressure derivative ($K'_{T0}$) are often discordant, even for samples with the same composition, preventing us from deciphering the effect of chemical substitutions on the elasticity of the CF-type phase. Ultimately, this hampers our ability to model the density and seismic velocities of basaltic phase assemblages at lower mantle conditions, which could be used to infer the presence of basaltic rocks by comparison with seismic observations (e.g., Kaneshima and Helffrich, 1999; Niu, 2014).

In a recent study, we showed how a multi-sample loading approach to high-pressure single-crystal X-ray diffraction (SCXRD) measurements in the DAC can help to reduce systematic differences and corroborate internal consistency between datasets collected on different samples (Criniti et al., 2024). This enables subtle differences in the unit-cell and structural parameters to be detected and compositional trends in the physical properties to be defined with higher precision. Here, this method has been adopted to investigate how chemical substitutions affect the crystal structure, polyhedral compressibility, and equation of state parameters of three CF-type samples synthesized in the $NaAlSiO_4$, $NaAlSiO_4$-$MgAl_2O_4$, and $NaAlSiO_4$-$MgAl_2O_4$-$Fe_3O_4$ systems. Compositional trends found here are then used to validate the suite of elastic parameters used for various CF-type end members in most recent thermodynamic databases.

## 2. Experimental methods

### 2.1. Sample synthesis and characterization

The CF-type samples employed in this study were synthesized and characterized by Ishii et al. (2023). The samples were obtained by annealing synthetic $NaAlSiO_4$ nepheline, synthetic $MgAl_2O_4$ spinel and reagent grade $Fe_3O_4$ mixed in different molar ratios at 23–24 GPa and 2273–2473 K in a Kawai-type multi-anvil apparatus. Their chemical compositions, determined by electron probe microanalyses (EPMA) and conventional Mössbauer spectroscopy, are $Na_{0.90(1)}Al_{1.03(2)}Si_{1.00(2)}O_4$ (H5477, NaCF), $Na_{0.66(4)}Mg_{0.28(4)}Al_{1.22(3)}Si_{0.78(3)}O_4$ (S7759, MgCF) and $Na_{0.62(2)}Mg_{0.19(1)}Fe^{2+}_{0.17(1)}Fe^{3+}_{0.080(4)}Al_{1.20(3)}Si_{0.70(1)}O_4$ (H5469, FeCF) (Ishii et al., 2023). Note that, in agreement with previous studies (e.g., Ono et al., 2009; Wu et al., 2017), cation vacancies were detected by both chemical analyses and X-ray structural refinement and were argued to concentrate in the 8-fold coordinated A site. For a more detailed description of the synthesis and characterization procedures, the reader is referred to our previous publication (Ishii et al., 2023).

### 2.2. Sample and diamond anvil cell preparation

Four compression experiments (Table 1) were performed employing BX90-type DACs (Kantor et al., 2012). The DACs were equipped with conical WC seats having opening angles of 90° and Almax-Boehler diamond anvils (Boehler and De Hantsetters, 2004), achieving an overall X-ray opening angle of up to 80°. Two of the four DACs employed in our experiments (Table 1) were also equipped with external resistive heaters consisting of a cylindrical ceramic component wrapped in Pt-wire (Pamato et al., 2016; Criniti et al., 2024). Here, however, only the room-temperature data collected in those runs will be presented, as high-temperature measurements are still underway and will be reported in a future publication. To create the sample chambers, rhenium gaskets were first indented to a thickness of approximately 50 or 30 μm depending on the culet size (i.e., 350 μm or 150 μm) and then laser-drilled to form cylindrical cavities acting as pressure chambers. Extreme care was taken in selecting the best crystals and most favorable orientations in order to maximize data coverage on all three crystallographic axes, which is often a problem in high-pressure experiments due to the shielding of the DAC body on the incident and diffracted X-rays. Further details on the sample selection are provided in the Supplementary Material 1 (Text S1).

One (run 2) or two (runs 1, 3, and 4) crystals with different compositions were loaded in each sample chamber together with a ruby sphere acting as a pressure standard (Shen et al., 2020) and a piece of nanocrystalline gold used to align the DAC at each pressure point by measuring its X-ray absorption profiles (Table 1, Fig. 1a-b). For runs 1 and 2, pre-compressed helium (He) at 0.13 GPa was loaded as quasi-hydrostatic pressure transmitting medium using the gas loading systems installed at the Bayerisches Geoinstitut, University of Bayreuth (Kurnosov et al., 2008) and at the PETRA-III synchrotron. Runs 3 and 4 were designed to achieve combined high-pressure and high-temperature conditions, therefore neon (Ne) was preferred as a pressure transmitting medium as it reduces the risk of anvil and gasket failure at high temperatures.

### 2.3. Single-crystal X-ray diffraction and structural refinements

SCXRD measurements at high pressure and room temperature were carried out at the P02.2 beamline of PETRA-III (Liermann et al., 2015). All measurements were conducted using a beam of 42.7 keV, corresponding to 0.2905 Å, that was focused down to 8 μm × 2 μm (full width at half maximum) using Be compound refractive lenses. Intensities were recorded on a Perkin Elmer XRD 1621 flat panel detector. The sample-to-detector distance was calibrated using polycrystalline $CeO_2$ and a single crystal of natural enstatite was employed to refine the instrument parameters for SCXRD measurements. Gas-driven membranes were used

**Table 1**
Diamond anvil cell (DAC) details and achieved experimental conditions.

| Run | Sample(s) | Pressure medium | Culet size (μm) | *P* sensor (s) | *P* range (GPa) |
|---|---|---|---|---|---|
| 1 | NaCF, MgCF | He | 350 | Ruby, Au | 1–50 |
| 2 | FeCF | He | 150 | Ruby | 22–72 |
| 3 | NaCF, FeCF | Ne | 350 | Ruby, Au | 3–35 |
| 4 | NaCF, FeCF | Ne | 350 | Ruby, Au | 10–35 |

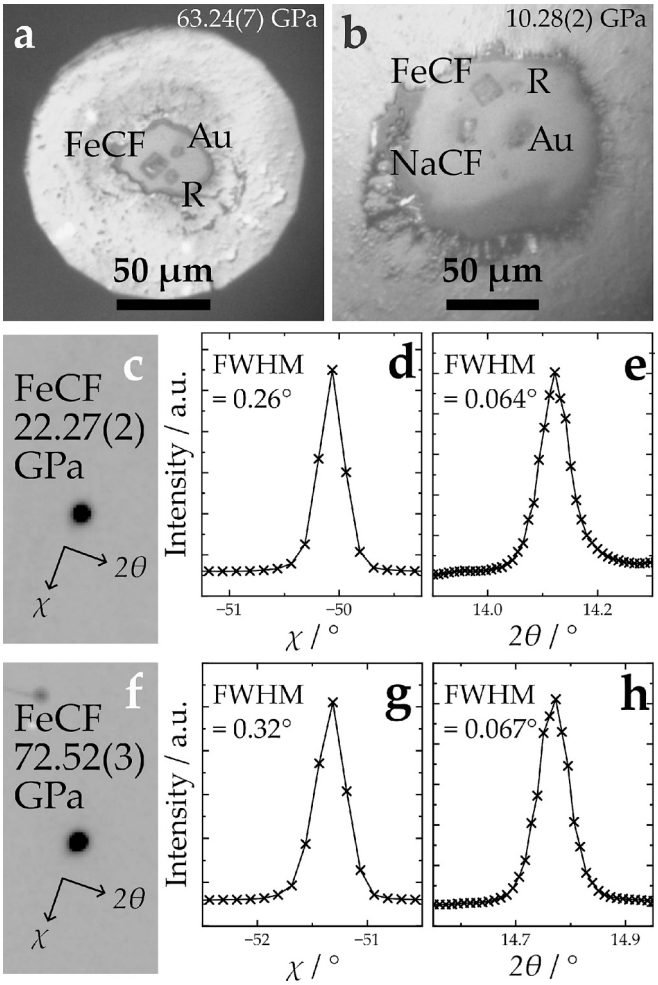


**Fig. 1.** (a-b) Optical images of DAC sample chambers at high pressure with one or two crystals of CF-type phase together with a ruby sphere (R) and polycrystalline Au as pressure standards. (c-f) The (232) Bragg reflection of FeCF at the (c-e) lowest and (f-h) highest pressures recorded in run 2, viewed in (c,f) two-dimensional X-ray scans as well as (d,g) $\chi$ and (e,h) $2\theta$ diffraction profiles.

to compress the DACs online while pressure in the sample chamber was monitored using an online ruby luminescence system. Ruby luminescence spectra were collected before and after every measurement and shifts of the ruby R1 line were converted to pressures using the calibration of Shen et al. (2020). X-ray diffraction measurements were conducted up to a maximum pressure of 50.15(2) GPa (NaCF, MgCF) or 72.52(3) GPa (FeCF). At each pressure point, step-scan images were collected while rotating the DAC about its vertical axis (ω) between ± 35°, ± 32° or ± 30° depending on the shadowing effect of the membrane cup on the incident and diffracted beams. Diffraction images were collected every 0.5° and exposure times varied between 0.5 s and 2 s depending on the size of the sample. *CrysAlisPro* (Oxford Diffraction, Rigaku) was used to harvest and index the sample reflections from each dataset and extract their unit-cell lattice parameters. Subsequently, intensity data were extracted after background subtraction, correction for Lorentz and polarization factors, frame scaling, and empirical absorption correction based on spherical harmonics using the ABSPACK algorithm implemented in *CrysAlisPro*. The high quality of the single crystals was preserved up to the maximum pressure achieved, as shown by the round shape of reflections in two-dimensional X-ray scans and the sharp rocking curves in both the chi ($\chi$) and two theta ($2\theta$) directions (Fig. 1c-h). The unit-cell lattice parameters are provided in the Supplementary Material 2.

Room-pressure structural refinements of the same samples reported in our previous publication (Ishii et al., 2023) were used as starting structural models for the NaCF and MgCF samples. In the high-pressure refinements, site occupancy factors (s.o.f.) and atoms per formula unit (a.p.f.u.) were fixed to the values obtained from the room pressure refinements (Ishii et al., 2023), as reported in Supplementary Material 1 (Table S1). For the FeCF sample, we used the intensity data at ambient conditions reported by Ishii et al. (2023) to refine a new structural model with fewer free parameters, aiming to reduce the correlation between s.o.f.'s of $Fe^{2+}$ and $Fe^{3+}$ in the different crystallographic sites. We first assumed $Al^{3+}$, $Si^{4+}$, and $Fe^{3+}$, whose concentrations were determined by EPMA and Mössbauer measurements [Al = 1.20(3) a.p.f.u., Si = 0.70(1) a.p.f.u., Fe = 0.25(1) a.p.f.u., $Fe^{3+}/\Sigma Fe$ = 0.32(1)], to only partition in the B1 and B2 sites. As the resulting occupancy of the octahedral sites would amount to 1.98 instead of 2.00, a $Mg^{2+}$ content of 0.01 per octahedral site was also assumed. The remaining $Mg^{2+}$ and $Fe^{2+}$ fractions were assigned to the A site. The occupancies of $Na^{+}$ (A site) and $Si^{4+}$, $Al^{3+}$, and $Fe^{3+}$ (B1 and B2 sites) were set as free variables and restraints on the chemical compositions based on EPMA measurements were applied. This new strategy significantly reduced the correlation between the s.o.f.'s of $Fe^{2+}$ and $Fe^{3+}$ in the different cation sites without significant changes in the crystallographic *R* factors and goodness of fit of the refinement. The resulting s.o.f. and a.p.f.u. can be found in in the Supplementary Material 1 (Table S1). The newly determined s.o.f.'s for FeCF sample were then fixed in the structural refinements at high pressure.

*SHELXL* in the *Shelxle* GUI (Hübschle et al., 2011; Sheldrick, 2015) was used to refine the atomic coordinates and displacement parameters of the samples at high pressure. The atomic parameters were refined against $F^2$ (with *F* being the structure factor) and neutral scattering factors were used for all atoms. The large openings of the DACs employed in this study allowed relatively high ratios of observed reflections (*r*) over refined parameters (*p*) to be obtained and anisotropic displacement parameters (ADPs) to be refined for all samples at all pressures. Isotropic displacement parameters were preferred only for the NaCF sample at 35.18(4) GPa, where the same ADP component of several atoms in the asymmetric unit was found to be close to zero, which was deemed unphysical. The resulting *r/p* values were found to range between 13.6 and 8.2, mainly depending on pressure and on the orientation of the crystal in the DAC. The refined structural models proved to be of high quality, with typical crystallographic *R*1 factors below 5 %, except for the NaCF and FeCF samples at some pressure points in runs 3 and 4 (Supplementary Material 1, Table S2). CIFs obtained from all structural refinements are provided as Supplementary Material 3-5.

## 3. Results and discussion

### 3.1. Volume compressibility

The high-pressure volume compression behavior of the three CF-type samples investigated in this study is shown in Fig. 2. Samples with Fe-free compositions displayed a smooth volume decrease over the entire pressure range investigated and their compression behavior is well described by 3rd-order Birch-Murnaghan (BM3) equations of state (EOS) (Angel et al., 2014; Birch, 1947). EOS fitting was performed through a weighted least square inversion using a script implemented in OriginPro2022 (OriginLab corporation, Northampton, MA, USA) and previously benchmarked against the EoSFit7 program (Angel et al., 2014; Gonzalez-Platas et al., 2016). The fitted zero-pressure volume ($V_0$), isothermal bulk modulus ($K_{T0}$), and its pressure derivative ($K'_{T0}$) are reported in Table 2, whereas the full covariance matrices obtained from each fit can be found in Supplementary Material 1 (Table S3). Differences between measured and calculated pressures were typically within 1 GPa (Supplementary Material 1, Fig. S2), confirming a good data reproducibility over the different runs.

The Fe-bearing sample, on the other hand, exhibits a region of

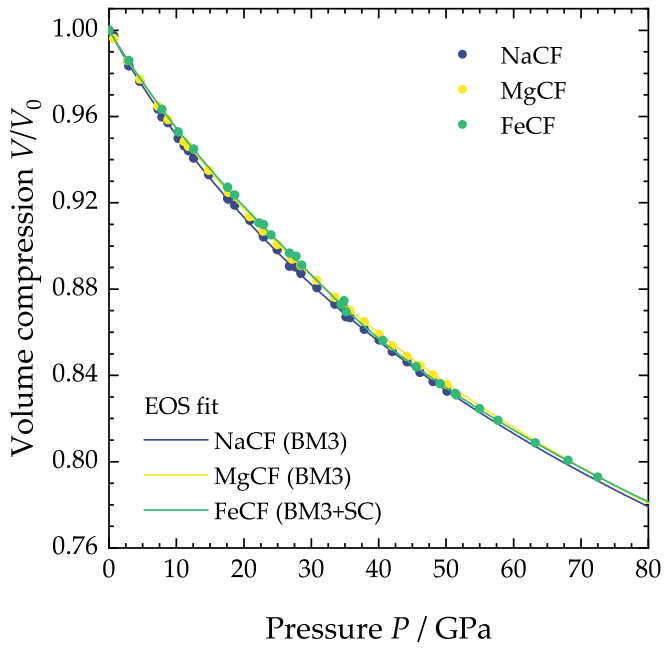


**Fig. 2.** Compression behavior of NaCF, MgCF, and FeCF normalized to their fitted $V_0$ (see Table 2). Filled circles indicate data points collected in this study over one (MgCF) or three (NaCF, FeCF) runs (Table 1), whereas lines indicate BM3 EOSs or the modified BM3 EOS accounting for the spin crossover of $Fe^{3+}$ (BM3 + SC). Error bars are smaller than the symbols and thus not displayed.

**Table 2**
EOS fit parameters of CF-type samples determined in this study. Note that the *b* and *c* fit parameters of the spin crossover EOS (BM3 + SC) are defined in Eq. (1) and are not the same as the *b* and *c* unit-cell lattice parameters.

| BM3 | | | | BM3 + SC | |
|---|---|---|---|---|---|
| Sample | NaCF | MgCF | FeCF | Sample | FeCF |
| *P* range (GPa) | 0–50.2 | 0.7–50.2 | 0–30 | *P* range (GPa) | 0–72.5 |
| $V_0$ (Å$^3$) | 240.77(3) | 239.99(5) | 242.13(2) | $V_0$ (Å$^3$) | 242.13 (2) |
| $K_{T0}$ (GPa) | 178.5(15) | 193.1(12) | 197(3) | $K_{T0}$ (GPa) | 194.8 (12) |
| $K'_{T0}$ | 4.66(12) | 4.14(6) | 4.0(2) | $K'_{T0}$ | 4.42(7) |
| $a_0$ (Å) | 10.1450 (11) | 10.1002 (11) | 10.1209 (10) | $\Delta_0$ | *14,750* |
| $M_{a0}$ (GPa) | 464(5) | 520(5) | 537(18) | $B_0$ | 651(10) |
| $M'_{a0}$ | 15.9(4) | 14.4(3) | 13.7(18) | $\delta$ | 5.1(3) |
| $b_0$ (Å) | 8.6728(6) | 8.6331 (14) | 8.6408(5) | $b = c$ | *−2* |
| $M_{b0}$ (GPa) | 410(5) | 503(6) | 511(10) | $C/B$ | *4.73* |
| $M'_{b0}$ | 15.1(5) | 11.2(3) | 12.7(10) | | |
| $c_0$ (Å) | 2.7374(3) | 2.7524(3) | 2.7687(3) | | |
| $M_{c0}$ (GPa) | 893(13) | 777(7) | 785(20) | | |
| $M'_{c0}$ | 8.2(6) | 11.0(3) | 8.4(15) | | |

slightly enhanced compressibility between approximately 30 and 40 GPa. This is apparent if the datapoints below 30 GPa are fitted with a BM3 EOS that is then extrapolated to higher pressures. Observed pressures and calculated pressures from the extrapolated BM3 EOS are found to diverge above 30 GPa before starting to slowly converge above 50 GPa (Supplementary Material 1, Fig. S3). This behavior can be ascribed to the pressure-induced spin crossover of $Fe^{3+}$ in octahedral coordination, as previously reported by Wu et al. (2017). A similar behavior was also observed in the high-pressure evolution of the octahedral B-site volume but not of the A-site volume, as will be discussed later. In order to account for the variation of the Helmholtz free energy (and thus pressure) due to a change in the electronic configuration of $Fe^{3+}$ ions, the EOS proposed by Buchen (2021) was adopted. The unique feature of this EOS is that only one set of parameters (i.e., $V_0$, $K_{T0}$, $K'_{T0}$) is required to calculate the elastic contribution to the total pressure of both high-spin and low-spin phases. The electronic contribution, on the other hand, is modelled by imposing a volume dependence on the crystal field parameters that are then used to calculate the free energy associated with each electronic state:

$$\Delta = \Delta_0 \left(\frac{V_0}{V}\right)^{\frac{\delta}{3}}, B = B_0 \left(\frac{V_0}{V}\right)^{\frac{b}{3}}, C = C_0 \left(\frac{V_0}{V}\right)^{\frac{c}{3}} \quad (1)$$

where $\Delta$ is the crystal field splitting, $B$ and $C$ are Racah parameters accounting for inter-electronic repulsions between *3d* electrons, the exponents $\delta$, $b$, and $c$ are adjustable parameters, and the subscript zero indicates values at the reference conditions (i.e., room pressure and temperature). A complete description of the model is presented in Buchen (2021) and summarized in the Supplementary Material 1 (Text S2).

In the case of the FeCF sample, only $B_0$ and $\delta$ were fitted, whereas the other parameters were assumed to be identical to those determined for octahedrally coordinated $Fe^{3+}$ in other oxide compounds (Krebs and Maisch, 1971; Lehmann and Harder, 1970). This proved to be sufficient to obtain a satisfactory fit of the observed pressure-volume data, as shown by the fit residual in Supplementary Material 1 (Fig. S2). Elastic and crystal field parameters were obtained through a weighted least square inversion performed in OriginPro2022, as described for the fitting of the conventional BM3 EOSs. The refined EOS fit parameters are reported in Table 2, whereas the full covariance matrix is provided in Supplementary Material 1 (Table S3). From the fit parameters, it is possible to calculate the fraction of high-spin ($^6A_1$) and low-spin ($^2T_2$) electronic states through eqs. S1-S8 in the Supplementary Material 1 (Text S2), as shown in Fig. S4. As the modelled unit-cell volume changes more markedly when $0.1 < \phi(^2T_2) < 0.9$, we evaluated that the spin crossover region extends from approximately 26 to 42 GPa. Note also that the data points in the $Fe^{3+}$ low-spin region also contribute to constraining the crystal-field parameters that define the elastic behavior of the sample across the spin crossover. This helps to reduce the uncertainty on the EOS across the entire investigated pressure range despite the slightly wider sampling interval of datapoints in the $Fe^{3+}$ spin crossover region.

### 3.2. Axial compressibility

From the analysis of the high-pressure evolution of the unit-cell lattice parameters of the CF-type crystals it is possible to obtain some insights on their anisotropic elastic properties. For this purpose, linearized BM3 EOSs (e.g., Angel et al., 2014; Criniti et al., 2024) were used to fit the linear compression data for the three compositions investigated here (Fig. 3a-c) from which the room-pressure axial moduli ($M_{l0}$) and their pressure derivatives ($M'_{l0}$) were refined (Table 2). For the NaCF and MgCF samples, the full dataset was used and all linearized EOSs interpolate well the experimental datapoints (Fig. 3a-b). For the FeCF sample, only data points before the onset of the spin-crossover (i.e., below 30 GPa) were considered as the spin-crossover formalism proposed by Buchen (2021) is only valid for volume compression data. The onset of the spin-crossover is most evident for the *a*-axis, which systematically deviates from the extrapolated EOS, and less significant for the *b*- and *c*-axes (Supplementary Material 1, Fig. S3).

The linear compressibility ($\beta_l$) can be calculated from the linearized EOS as the inverse of the axial modulus ($M_l$). Fig. 3d shows how the calculated $\beta$ values for the three CF-type samples evolve as a function of pressure. As already predicted by first-principle calculations (Kawai and Tsuchiya, 2012; Kawai and Tsuchiya, 2010; Mookherjee, 2011; Yin et al., 2012), the elasticity of the CF-type structure is significantly anisotropic in the low-pressure range. Our results show that the *c*-axis is the stiffest direction and the *a*- and *b*-axes have higher and somewhat

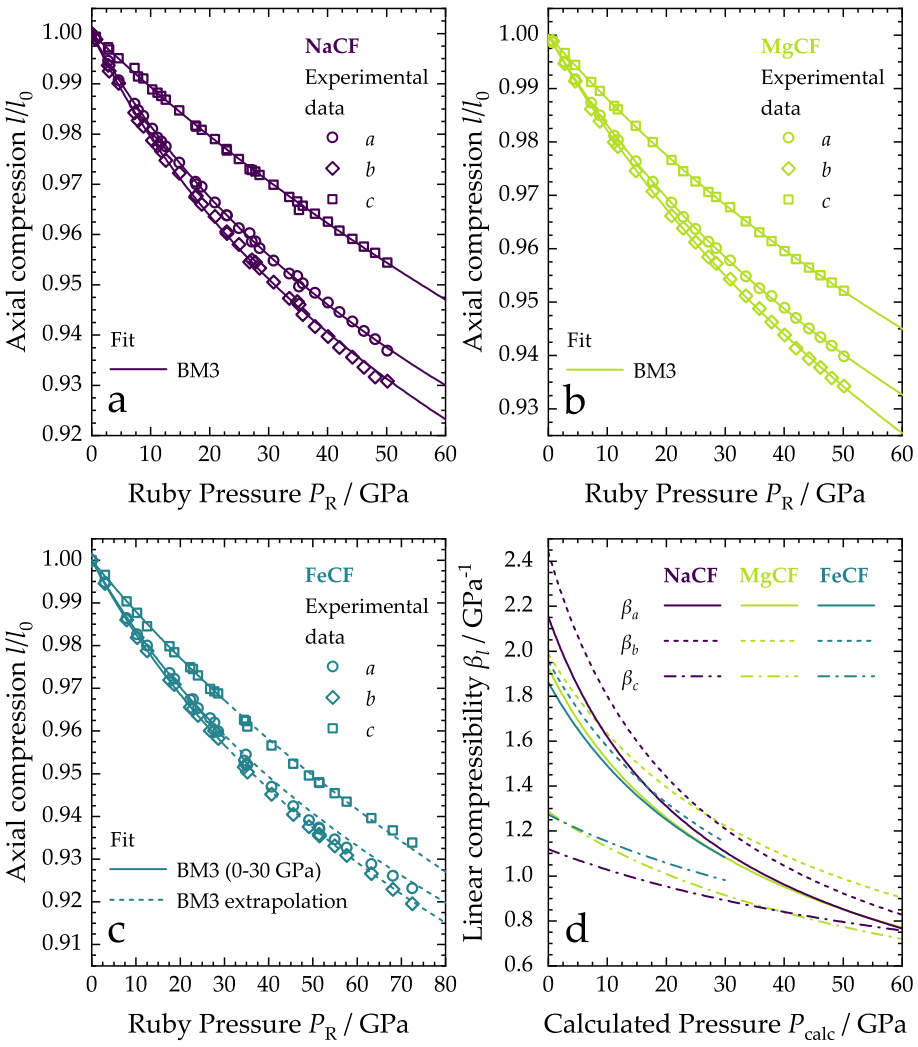


**Fig. 3.** (a-c) Axial compression behavior of (a) NaCF, (b) MgCF, and (c) FeCF normalized to the fitted $l_0$ values (Table 2). Solid lines represent linearized BM3 EOSs fit using (a-b) the full dataset or (c) data up to 30 GPa, before the onset of the $Fe^{3+}$ spin crossover. Dashed lines in (c) are extrapolated linearized EOS showing an increase in compressibility above ~30 GPa, particularly for the *a*-axis (see also Supplementary Material 1, Fig. S3). Error bars are smaller than the symbols and thus not displayed. (d) Calculated axial compressibility curves for the three CF-type samples as a function of pressure. Curves for the FeCF sample are limited to 30 GPa, where $Fe^{3+}$ is in the high-spin state.

similar compressibility (Fig. 3d). With increasing pressure, the compressional anisotropy tends to decrease, whereas the compressibility scheme $\beta_b > \beta_a > \beta_c$ is retained up to at least 50 GPa. This is in contrast with a recent SCXRD study on CF-type $Na_{0.93}Al_{1.02}Si_{1.00}O_4$ and $Na_{0.88}Fe_{0.13}Al_{0.99}Si_{0.94}O_4$, which suggested $\beta_a > \beta_b > \beta_c$ at ambient conditions (Qin et al., 2023). It can also be seen that the NaCF sample, although more anisotropic than the other two at ambient conditions, shows similar compressibility values above ~25 GPa, which is approximately the pressure at which the CF-type phase becomes stable in a metabasaltic phase assemblage (e.g., Ishii et al., 2019). Therefore, we can expect chemical substitutions to have limited effects on the elastic anisotropy of the CF-type phase, at least in the topmost lower mantle.

### 3.3. A-site compressibility

The A site of the CF-type structure, hosting $Na^+$, $Mg^{2+}$, and $Fe^{2+}$, is coordinated by eight oxygen atoms forming four relatively short bonds with O2 and O3 and four longer bonds with O1 and O4 (Supplementary Material 1, Fig. S1), each metal-oxygen bond responding differently to changes in pressure and chemical composition. Experimentally determined A-O bonds as a function of pressure are plotted in Fig. 4a-c for the three CF-type samples investigated here together with their linearized BM3 EOS, for which the EOS fit parameters are reported in Supplementary Material 1 (Table S4). The most compressible bond is A-O1 ($M_0$ = 333–346 GPa, see Supplementary Material 1, Table S4), which is parallel to the *a*-*c* plane, despite the *a*- and *c*-axes being less compressible than the *b*-axis. This is true for all samples, despite the fact that substituting $Na^+$ in the A site with $Mg^{2+}$ and $Fe^{2+}$ seems to decrease the room-pressure value of A-O1 (Fig. 4a-c). The enhanced compressibility of A-O1 cannot be explained by a shrinking of the unit cell edges alone but can be attributed to the shift of the A-site cation along the *a*-axis and towards the O1 atom as pressure increases. On the other hand, the two shorter interatomic distances, A-O3 ($M_0$ = 419–510 GPa) and A-O2 ($M_0$ = 409–480 GPa), which have a more relevant component parallel to the stiffer *c*-axis, are less compressible. Moreover, all A-O bonds except for A-O1 become less compressible as $Mg^{2+}$ and $Fe^{2+}$ are incorporated in the A site. The overall site distortion can be calculated as $D = \frac{1}{n}\sum_{i=1}^{n}\left|\frac{d_i}{d_{av}} - 1\right|$, where $d_{av}$ is the average < A-O > interatomic distance and $n$ is the coordination number (i.e., 8 for the A site). Due to the abovementioned subtle differences in the compressibility of the individual bonds, the A-site distortion ($D^A$) tends to decrease with increasing pressure (Supplementary Material 1, Fig. S5). This was not captured by the recent experimental study of Qin et al. (2023), who observed a

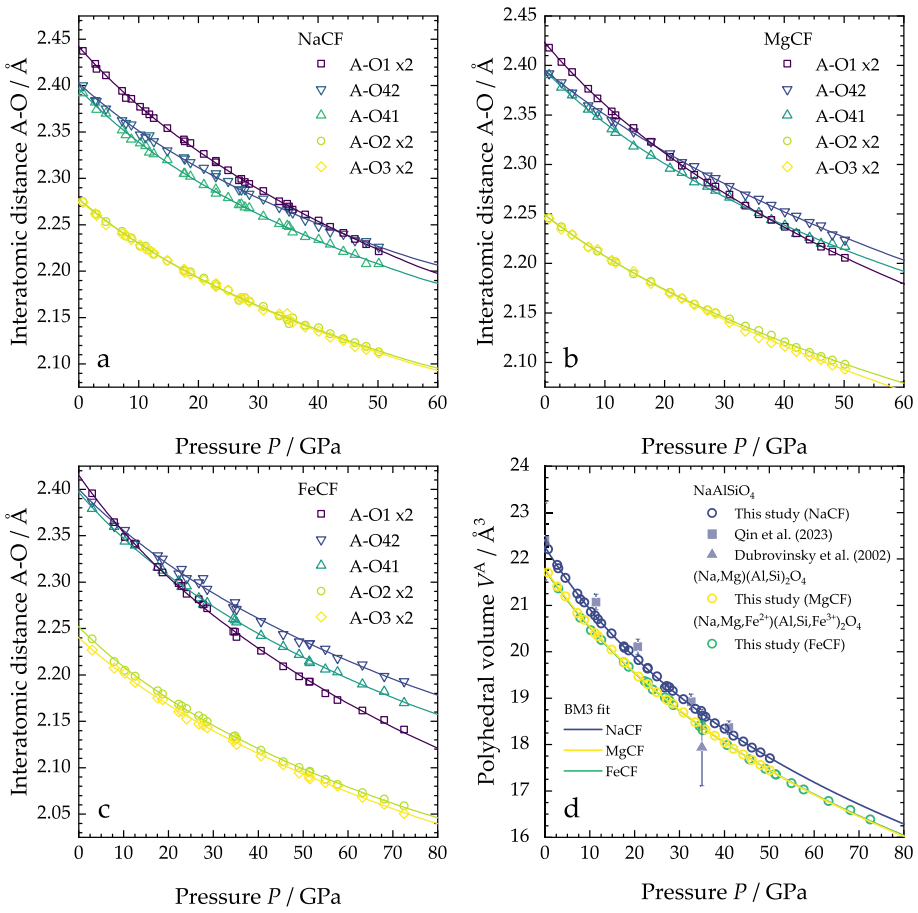


**Fig. 4.** Pressure evolution of individual A-O interatomic distances for (a) NaCF, (b) MgCF, and (c) FeCF, and (d) of their polyhedral volume ($V^A$). The reader is referred to Supplementary Material 1 (Fig. S1) for individual bond labels. Lines are BM3 EOS fits to the experimental data. Previous studies on the $NaAlSiO_4$ end member are also shown in (d) for comparison. Error bars are smaller than the symbols where not displayed.

virtually constant $D^A$ in their $NaAlSiO_4$ CF-type sample between 0 and 40 GPa, perhaps due to the large scatter of their data.

Fitting BM3 EOSs to the pressure-A-site-volume ($P$-$V^A$) datasets (Fig. 4d) allows information on the A-site bulk modulus ($K_0^A$) and its pressure derivative ($K^{A}{}'_0$) to be retrieved (Table 3). This is important as determining the polyhedral compressibility of CF-type phases with different compositions can help to deconvolute the effects of individual cation substitutions on the bulk compressibility of complex solid solutions. Similar to the distortion index, the $P$-$V^A$ trends defined by the MgCF and FeCF are virtually the same, which is reflected in BM3 fit parameters being the same within uncertainty, even considering the correlation between $K_0^A$ and $K^{A}{}'_0$ (Fig. 5a) and in spite of the different occupancies for this site. On the other hand, the lower $K_0^A$ value displayed by the NaCF sample is not canceled out by the increase in $K^{A}{}'_0$ as revealed by the analysis of the covariance ellipses (Fig. 5a). This suggests that the main factor controlling the A-site compressibility is the $Na^+$ content, whereas the effect of the $Mg^{2+}$ and $Fe^{2+}$ substitutions are very similar and seem to only influence the compression behavior of some interatomic distances. It should also be noted that there seems to be no effect of the $Fe^{3+}$ spin-crossover taking place in the B sites on the compression behavior of the A site, as this is well described by the conventional BM3 EOS formalism over the entire pressure range investigated.

**Table 3**
3rd-order Birch-Murnaghan and spin-crossover equations of state parameters for the polyhedra of the three CF-type samples.

| | NaCF | MgCF | FeCF[a] |
|---|---|---|---|
| $V_0^A$ | 22.256(17) | 21.789(8) | 21.77(3) |
| $K_0^A$ | 143(2) | 152.8(14) | 153(4) |
| $K^{A}{}'_0$ | 3.74(11) | 3.53(7) | 3.61(12) |
| $V^{B1}0$ | 8.427(7) | 8.503(5) | 8.624(11) |
| $K_0^{B1}$ | 260(7) | 257(6) | 259(12) |
| $K^{B1}{}'_0$ | 4.4(3) | 4.7(3) | 5.1(5) |
| $B_0^{B1}$ | – | – | 585(16) |
| $\delta^{B1}$ | – | – | 4.0(6) |
| $V_0^{B2}$ | 8.556(8) | 8.669(7) | 8.841(11) |
| $K_0^{B2}$ | 232(8) | 251(8) | 270(12) |
| $K^{B2}{}'_0$ | 6.3(5) | 5.1(4) | 5.1(5) |
| $B_0^{B2}$ | – | – | 571(9) |
| $\delta^{B2}$ | – | – | 3.1(3) |

[a] Crystal-field parameters for the spin-crossover equation of state other than $B_0$ and $\delta$ (i.e., $\Delta_0$, $b$, $c$, and $C/B$) are the same as reported in Table 2.

### 3.4. B-site compressibility

The pressure evolution of the individual B–O interatomic distances for the B1 and B2 octahedral sites of all CF-type samples is reported in Fig. 6 together with linearized BM3 EOS fits for the entire pressure range investigated (NaCF and MgCF) or up to 30 GPa (FeCF) to avoid contributions from the $Fe^{3+}$ spin crossover (Supplementary Material 1, Table S5). Occupancy factors refined from single-crystal diffraction data are reported in Supplementary Material 1 (Table S1). As already observed by Ishii et al. (2023) there seems to be a preference for trivalent cations to occupy the B2 site [$(Al + Fe^{3+})/(Si + Al + Fe^{3+}) = 0.57–0.71$, Supplementary Material 1, Table S1], whose polyhedral volume is consistently larger than the B1 site at ambient conditions, whereas $Si^{4+}$ partitions preferentially into the smaller B1 site

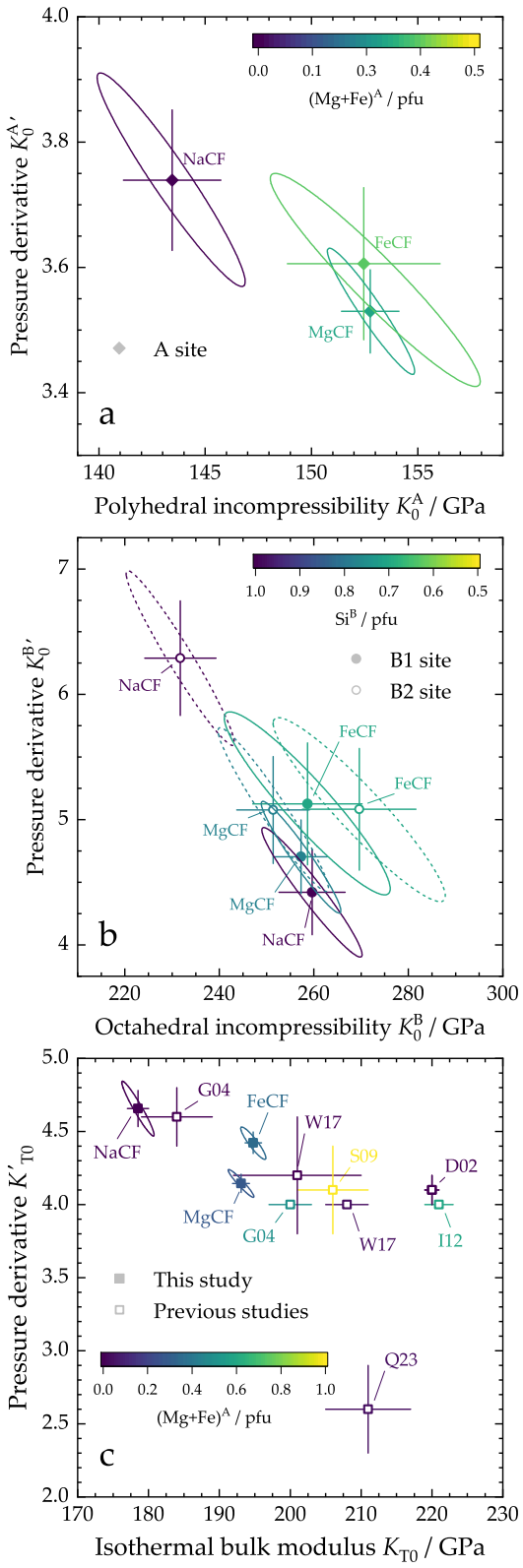


**Fig. 5.** $K_0$-$K'_0$ relations for the (a) A site, (b) B sites, and (c) bulk CF-type structure obtained from 3rd-order Birch-Murnaghan equations of state fitted to experimental data. One-standard-deviation covariance ellipses are shown as solid or dashed lines for samples from this study. The color coding is used to indicate differences in chemical composition among the samples. In (c), labels are used to indicate previous experimental studies: Dubrovinsky et al. (2002) (D02); Guignot and Andrault (2004) (G04:); Sueda et al. (2009) (S09); Imada et al. (2012) (I12); Wu et al. (2017) (W17); Qin et al. (2023) (Q23).

$[(Al^{3+}+Fe^{3+})/(Si^{4+}+Al^{3+}+Fe^{3+}) = 0.42–0.56$, Supplementary Material 1, Table S1]. In both octahedra, the longest interatomic distances at ambient conditions are the two apical bonds which lie perpendicular to the *c*-axis (Supplementary Material 1, Fig. S1). In general, the interatomic distances and bond compressibility are expected to increase with the trivalent cation content due to the larger ionic radii of $Al^{3+}$ and $Fe^{3+}$ compared to $Si^{4+}$ (Shannon, 1976). While this is true for the equatorial bonds of all samples (Supplementary Material 1, Table S5), the apical bonds do not always follow the same trend as the non-equatorial edges of the octahedra are often shared with the two "caps" of the A-site polyhedron and, therefore, are more influenced by the volume and compressibility of the A site, and thus by its chemistry. This explains why both the interatomic distances and bond compressibility of B1-O2 and B2-O4 are larger in samples with higher $Si^{4+}$ (B sites) and $Na^{+}$ (A site) contents, and decrease with increasing bulk $Mg^{2+}$, $Fe^{2+}$, and $Al^{3+}$ content (Supplementary Material 1, Table S5). The difference in linear compressibility between apical and equatorial bonds displayed by both B sites causes the distortion indices $D^{B1}$ and $D^{B2}$ to drop significantly with increasing pressure, especially for the NaCF and MgCF samples (Supplementary Material 1, Fig. S5). The FeCF, on the other hand, shows a decrease of both octahedral distortions up to approximately 25 GPa, followed by a subtle increase in $D^{B1}$ and a more pronounced increase in $D^{B2}$ after the onset of the spin crossover (Supplementary Material 1, Fig. S5). Further crystallographic considerations on the anisotropic compression behavior of the B1 and B2 sites are provided in the Supplementary Material 1 (Text S3).

The high-pressure evolution of the octahedral volume for the three CF-type samples is shown in Fig. 7. BM3 EOSs were fit to $P$-$V^B$ dataset for the Fe-free composition, while the BM3 EOS corrected for the effect of the $Fe^{3+}$ spin-crossover (BM3 + SC) was employed to fit data from the FeCF sample. All curves interpolate the experimental data points well and the corresponding fit parameters are reported in Table 3. The compression behavior of the B1 site (Fig. 7a) is relatively similar among the three samples up to approximately 25 GPa, which may be due to the limited influence of the A site on the B1–O interatomic distances and the relatively similar site occupancy factors among the three samples (Supplementary Material 1, Table S6). Above this pressure and up to approximately 45 GPa, a slight increase in the compressibility of the B1 site of the FeCF sample is observed, which is compatible with the onset of the $Fe^{3+}$ spin-crossover and is well fitted by the BM3 + SC EOS introduced above. Above 45 GPa, $V^{B1}$ values of FeCF progressively diverge from those of NaCF and MgCF, highlighting a stiffening of the B1 site. In the case of the B2 site (Fig. 7b), the NaCF has a much lower site modulus than the other two compositions at room pressure but a higher pressure derivative, which is likely related to the low $M_0$ and high $M'_0$ values observed for the B2-O4 bond (Supplementary Material 1, Table S5) and the fact that B2 octahedra share two faces with the A-site polyhedron. This explanation seems more likely than a simple problem of high correlation between $K_0$ and $K'_0$, as the covariance ellipses for the B1 and B2 sites are well separated (Fig. 5b), as will be discussed later. The FeCF B2 site, which has the highest $K_0^B$ at ambient conditions, experiences bulk elastic softening between 25 and 45 GPa, similar to the B1 site but with a more significant volume collapse in a slightly narrower pressure interval. Above 45 GPa, the compressibility decreases again and the gap with the NaCF and MgCF data points widens. Both the magnitude of the volume collapse and the sharpness of the spin crossover are expected to increase with increasing $Fe^{3+}$ content, as shown for other lower mantle phases such as (Al,$Fe^{3+}$)OOH (e.g., Ohira et al., 2019; Strozewski et al., 2023; Thompson et al., 2020). This agrees well with the results obtained from our SCXRD structural refinement and by Ishii et al. (2023), suggesting that the concentration of $Fe^{3+}$ in the two sites is not the same, with $Fe^{3+}$ preferring the B2 site (Supplementary Material 1, Table S1). Note also that a tradeoff can be found between the fit parameters $B_0$ and $\delta$ for the B1 and B2 sites as well as for the bulk sample (Supplementary Material 1, Fig. S6), which again likely stems from the high correlation among these and other parameters during the

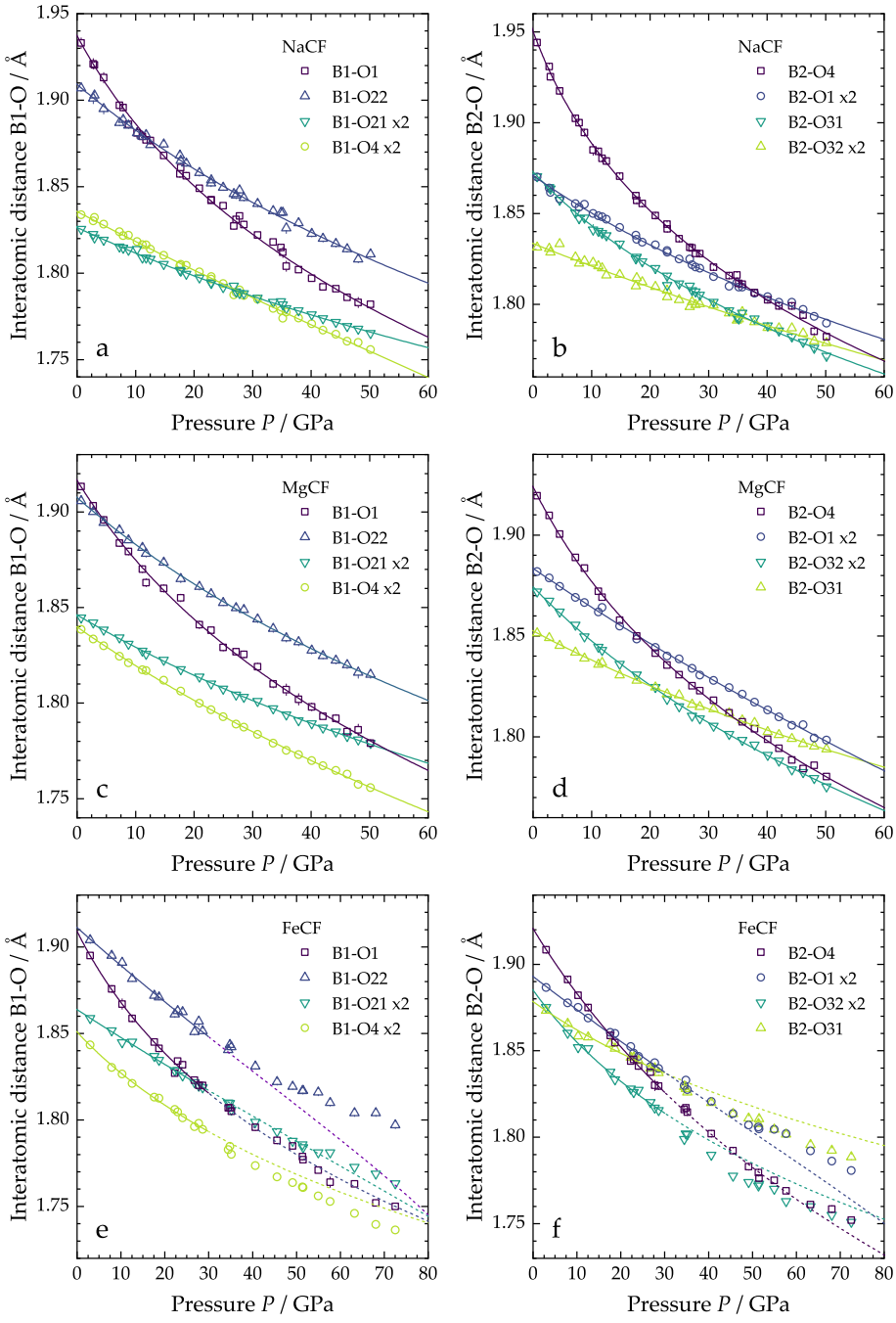


**Fig. 6.** Pressure evolution of individual B1–O and B2–O interatomic distances of (a,b) NaCF, (c,d) MgCF, and (e,f) FeCF. The reader is referred to Supplementary Material 1 (Fig. S1) for individual bond labels. Error bars are smaller than the symbols where not displayed.

fit of the experimental data as well as from the different $Fe^{3+}$ contents.

The B1 site EOS parameters (Fig. 5b) display minimal shifts, with $K^{B1'}{}_0$ slightly increasing with increasing trivalent cations content and $K_0^{B1}$ remaining practically constant within uncertainties. For the B2 site (Fig. 5b), the coupled substitution of $Al^{3+}$ in the B sites and $Mg^{2+}$ in the A site does shift the fitted $K_0^{B2}$ and $K^{B2'}{}_0$ relative to the NaCF sample but does not result in a significant stiffening or softening given the tradeoff between the two parameters, as highlighted by the covariance ellipses. For the FeCF sample, on the other hand, an increase in $K_0^{B2}$ with respect to MgCF is observed which does not translate in a decrease of $K^{B2'}{}_0$, making it overall less compressible (Fig. 5b). This behavior is somehow counterintuitive when the CF-type phase is compared to other lower mantle phases, such as bridgmanite and stishovite, where the addition of trivalent cations into octahedral sites dominated by $Si^{4+}$ tends to increase the octahedral compressibility (Criniti et al., 2024; Criniti et al., 2023). However, octahedra are not significantly distorted in bridgmanite and stishovite and remain undistorted upon compression and changes in the site chemical composition. The behavior displayed by the CF-type phase could therefore be related to the more distorted nature of its octahedral sites (Supplementary Material 1, Fig. S5) which likely arises from octahedra sharing edges and faces with the A site, for which a clearer influence of the chemical substitutions on the EOS parameters is observed (Fig. 5a).

### 3.5. *Effect of chemistry on the bulk compressibility of CF-type phase*

The information on the structural evolution of the investigated CF-type samples allows the effect of chemical substitutions at different

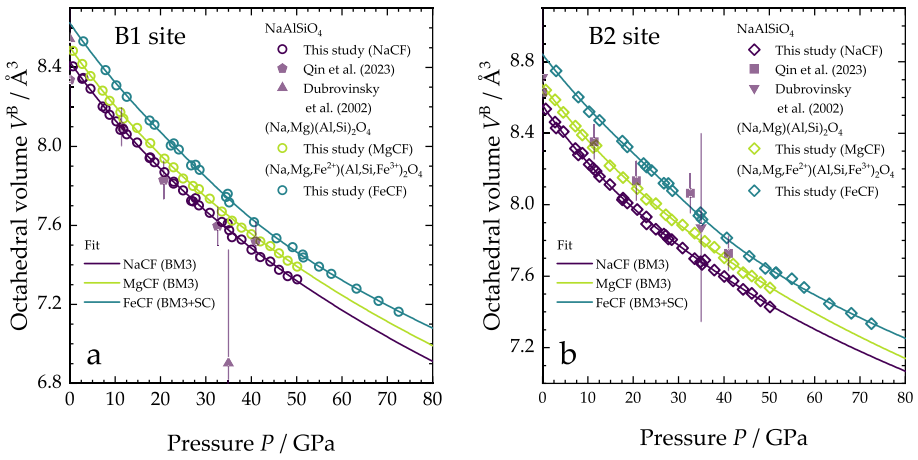


**Fig. 7.** $P$-$V^B$ relations for (a) the B1 and (b) the B2 octahedral sites of the three CF-type samples investigated here and of $NaAlSiO_4$ samples from previous studies (Dubrovinsky et al., 2002; Qin et al., 2023). Open symbols are experimental data points from this study and solid lines their respective BM3 (NaCF, MgCF) or BM3 + SC (FeCF) fits. Error bars are smaller than the symbols where not displayed.

crystallographic sites on the bulk compressibility of this material to be evaluated. The BM3 EOS fit parameters determined in this study indicate an overall stiffening of the CF-type structure with decreasing $NaAlSiO_4$ content. This effect was not obvious in previous experimental studies as the previously measured $P$–$V$ and $P$-$l$ data appear too scattered (Supplementary Material 1, Fig. S7), which is reflected in the wide range of proposed $K_{T0}$ and $K'_{T0}$ values (Fig. 5c and Supplementary Material 1, Table S6). Discrepancies in EOS parameters are often argued to be related to non-hydrostatic stress conditions in the sample chamber (Klotz et al., 2009) and to the use of pressure scales that are not intercalibrated (e.g., Fei et al., 2007). In this study, the use of a multi-sample loading strategy and the choice of He and Ne as pressure-transmitting media proved to be particularly effective as they reduced systematic discrepancies between datasets and enabled a more meaningful comparison between different samples to be made. The quality of the data is also shown by the high reproducibility of both unit-cell lattice parameters and structural data collected in several different runs for the NaCF and FeCF samples. The trend found in our study is in broad agreement with earlier powder diffraction measurements by Guignot and Andrault (2004) on $NaAlSiO_4$-$MgAl_2O_4$ solid solutions and by Sueda et al. (2009) on the $MgAl_2O_4$ end member, who found $K_{T0}$ to increase and $K'_{T0}$ to decrease with increasing $MgAl_2O_4$ content. Powder diffraction data on CF-type $Na_{0.4}Mg_{0.6}Al_{1.6}Si_{0.4}O_4$ (Imada et al., 2012) suggest a relatively high $K_{T0}$ value of 221(2) GPa (with $K'_{T0}$ fixed to 4) and thus a more pronounced stiffening due to $MgAl_2O_4$ incorporation. However, such a high $K_{T0}$ value could have resulted from the use of NaCl as pressure-transmitting medium or no pressure medium at all, both of which favor non-hydrostatic interaction between crystallites in the powdered sample. Wu et al. (2017) used single-crystal X-ray diffraction to examine an Fe-free and an Fe-bearing $NaAlSiO_4$ CF-type samples loaded in the same DAC and proposed $K_{T0}$ and $K'_{T0}$ values of 201–208 GPa and 4.0–4.2, respectively. The use of 2nd and 3rd-order Birch-Murnaghan EOS as well as scattering of the $P$–$V$ data makes it difficult to compare the fit parameters obtained for these two CF compositions. Therefore, we refitted the original data of Wu et al. (2017) using BM3 and BM3 + SC EOSs, and obtained the following fit parameters: $V_0 = 241(1)$ Å$^3$, $K_{T0} = 197(18)$ GPa, $K'_{T0} = 4.4(7)$ for the Fe-free sample; $V_0 = 243.1(3)$ Å$^3$, $K_{T0} = 197(5)$ GPa, $K'_{T0} = 4.0(2)$, $B_0 = 853(44)$ cm$^{-1}$, $\delta = 10(1)$ for the Fe-bearing sample. However, the overlapping EOS fit parameters and their large uncertainties, especially for the Fe-free sample, prevented us from obtaining better constraints on the effect of chemistry on the compressibility of the CF-type phase. The same two CF-type samples were also employed in a more recent SCXRD study where $K_{T0}$ values of 211–220 GPa and unusually low $K'_{T0}$ values of 2.6 were proposed (Qin et al., 2023). Especially for the Fe-bearing sample, the new dataset comprises fewer datapoints and has lower resolution in the low-pressure range, which are factors that can affect the EOS fit parameters during the inversion of $P$–$V$ data. Moreover, Qin et al. (2023) did not find any evidence for the $Fe^{3+}$ spin-crossover, which was, however, observed by both SCXRD (~25–40 GPa) and synchrotron Mössbauer spectroscopy (~25–35 GPa) on samples from the same batch in an earlier study (Wu et al., 2017). As materials are known to become softer in the pressure interval where the spin-crossover takes place, this could have contributed to the unusually low $K'_{T0}$ value for the Fe-bearing sample.

Results from first-principle calculations in the $NaAlSiO_4$-$MgAl_2O_4$ system also seem to point towards an increase in $K_0$ of ~20–25 GPa from $NaAlSiO_4$ to $MgAl_2O_4$ (Kawai and Tsuchiya, 2012, 2010; Mookherjee, 2011; Wang et al., 2020; Zhao et al., 2018), in agreement with experimental data from this study and Sueda et al. (2009). Similar to our experiments, computations also reported a mild decrease in $K'_0$ with increasing $MgAl_2O_4$ content (Kawai and Tsuchiya, 2012; Kawai and Tsuchiya, 2010; Mookherjee, 2011; Zhao et al., 2018). The effect of $Mg^{2+}$-$Fe^{2+}$ substitution in the A site was recently explored by computational methods (Wang et al., 2020). While $K$ values were only reported starting from 30 GPa, results suggest that the $Fe^{2+}Al_2O_4$ component could further reduce the compressibility of the CF-type phase. This trend is not captured by the fit parameters of the MgCF and FeCF samples reported here, although it could be masked by the effect of $Fe^{3+}$ incorporation in the B1 and B2 sites. Further experimental studies on the $MgAl_2O_4$-$Fe^{2+}Al_2O_4$ system will be needed to better understand the roles of ferric and ferrous iron on the structural and elastic properties of the CF-type phase.

## 4. Implications

Aluminous phases with the CF-type structure synthesized in dry basaltic systems are known to exhibit a complex crystal chemistry (Hirose et al., 2005; Hirose and Fei, 2002; Ishii et al., 2022, 2019; Ono et al., 2001; Ricolleau et al., 2010). Predicting and tracing changes in their thermodynamic and elastic properties as a function of pressure, temperature, and redox conditions is only possible by constraining the thermodynamic properties of an appropriate number of end-member components. However, some of these end-member compositions are known to break down into simple oxides at high pressure and temperature (Schollenbruch et al., 2010) or were found to crystallize with different post-spinel structural types (Ishii et al., 2020; Ricolleau and Fei, 2016; Schollenbruch et al., 2011), so that their properties cannot be directly measured. It follows that at least some of the end-member properties of CF-type solid solutions must be inferred by extrapolation of trends defined in relatively narrow compositional ranges. One

possible way around this problem is to make use of compositional trends in the polyhedral volumes and elastic properties. Previous studies found that mineral properties, such as compressibility, can be inferred from the relation between the ionic potential and the compressibility of their constituent atomic species (e.g., Hazen, 1988; Bruschini et al., 2015). A similar approach based on the polyhedral volume and assuming only site-specific substitutions (i.e., three site model) could be used to determine the end-member properties of a given atomic species *j* in the cation site *i* of the CF-type structure by fitting experimental data with the following equation:

$$K = \frac{\sum_i^{sites}\sum_j^{atoms} n_j^i V_j^i}{\sum_i^{sites}\sum_j^{atoms} \frac{n_j^i V_j^i}{K_j^i}} \quad (2)$$

where $n_{ij}$, $V_{ij}$, and $K_{ij}$ are the atomic fraction, polyhedral volume, and polyhedral bulk modulus associated with the atom *j* in the cation site *i* and *K* is the bulk modulus of the solid solution. Several CF-type end members differ from each other by only one cation per crystallographic site. For instance, understanding the effect of the Al-$Fe^{3+}$ exchange in the B sites would allow the end-member pairs $Na(Al,Fe^{3+})SiO_4$, $Mg(Al,Fe^{3+})_2O_4$, $Fe^{2+}(Al,Fe^{3+})_2O_4$, $Ca(Al,Fe^{3+})_2O_4$ to be simultaneously constrained. If complemented by further high-pressure structural data on more $Fe^{2+}$- and/or $Fe^{3+}$-rich samples, compositional trends found for $K^A$, $K^{B1}$, and $K^{B2}$ in this study will therefore help constraining the elastic properties of multiple CF-type phase end members both at room- and at high-pressure conditions.

The EOS parameters determined in this study can also be used to compare the high-pressure elastic properties of CF-type end members and solid solutions with those calculated from thermodynamic libraries used for mineral physical modeling (e.g., Stixrude and Lithgow-Bertelloni, 2011, 2022). As discussed above, our data indicate an increase in $K_{T0}$ and a slight decrease in $K'_{T0}$ with decreasing $NaAlSiO_4$ content, which is consistent with experimental results on the $MgAl_2O_4$ end member by Sueda et al. (2009) (Fig. 8a-b) and with computational studies (Kawai and Tsuchiya, 2012; Kawai and Tsuchiya, 2010; Mookherjee, 2011; Zhao et al., 2018). The database of Stixrude and Lithgow-Bertelloni (2022) employs similar end-member properties for $MgAl_2O_4$ but has a significantly higher $K_{T0}$ value for $NaAlSiO_4$ (Fig. 8a) as this value was derived from the early study of Dubrovinsky et al. (2002) who did not use any pressure transmitting medium in their DAC experiments. We make use of the $NaAlSiO_4$-$MgAl_2O_4$ system as a proxy to

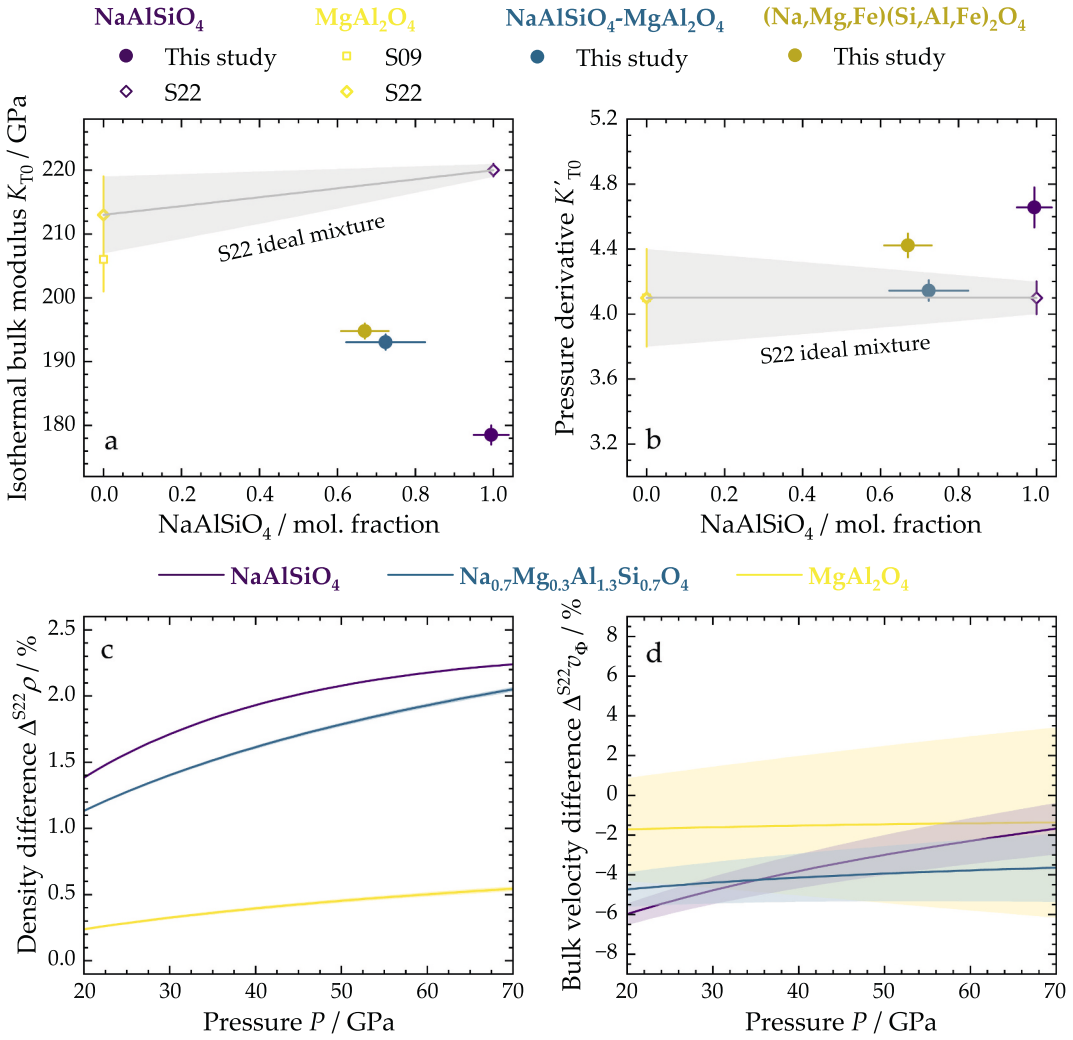


**Fig. 8.** (a-b) Compositional dependency of (a) the isothermal bulk modulus ($K_{T0}$) and (b) its pressure derivative ($K'_{T0}$) for CF-type phases. Solid gray lines and shaded areas represent $K_{T0}$ and $K'_{T0}$ ideal mixing models and propagated uncertainties across the $NaAlSiO_4$-$MgAl_2O_4$ join. (c-d) Calculated (c) density ($\Delta^{S22}\rho$) and (d) bulk sound velocity ($\Delta^{S22}v_\Phi$) differences between experimentally measured CF-type samples and the thermodynamic database of Stixrude and Lithgow-Bertelloni (2022) (S22) as a function of pressure. Experimental elastic parameters for the $NaAlSiO_4$, $Na_{0.7}Mg_{0.3}Al_{1.3}Si_{0.7}O_4$, and $MgAl_2O_4$ are taken from this study (NaCF, MgCF) and Sueda et al. (2009) (S09). Shaded areas are uncertainties propagated from the EOS parameters. Note that the larger errors on $\Delta^{S22}\rho$ and $\Delta^{S22}v_\Phi$ for the $MgAl_2O4$ end member arise from the larger errors on (a) $K_{T0}$ and (b) $K'_{T0}$ reported by both Sueda et al. (2009) and Stixrude and Lithgow-Bertelloni (2022).

quantitatively explore how differences in elastic parameters impact $\rho$ and $v_\Phi$ of the CF-type phase at pressures of the top- to mid-lower mantle (Fig. 8c-d and Supplementary Material 1, Fig. S8), where the presence of recycled oceanic crust with basaltic composition could explain the small-scale seismic velocities and density anomalies associated with seismic scatterers (e.g., Kaneshima and Helffrich, 2003; Niu, 2014; Kaneshima, 2019). For this purpose, we compare properties determined experimentally in this study (NaCF, MgCF) and by Sueda et al. (2009) with those calculated for $NaAlSiO_4$, $Na_{0.7}Mg_{0.3}Al_{1.3}Si_{0.7}O_4$, and $MgAl_2O_4$ from Stixrude and Lithgow-Bertelloni (2022) assuming an ideal mixing model. Differences in density ($\Delta^{S22}\rho$) and bulk sound velocity ($\Delta^{S22}v_\Phi$) are calculated according to:

$$\Delta^{S22}\rho = \frac{\rho_{exp} - \rho_{S22}}{\rho_{S22}} \times 100\% \quad (3)$$

$$\Delta^{S22}v_\Phi = \frac{v_{\Phi exp} - v_{\Phi S22}}{v_{\Phi S22}} \times 100\% \quad (4)$$

where subscripts indicate values determined experimentally (*exp*) or taken from Stixrude and Lithgow-Bertelloni (2022) (*S22*). We further restrict our calculations to room temperature as the only experimentally determined thermal parameters for CF-type phases are from Sueda et al. (2009) for the $MgAl_2O_4$ end member and those parameters are typically assumed to be the same for the other end members as well (e.g., Stixrude and Lithgow-Bertelloni, 2022). We calculate that the density difference ($\Delta^{S22}\rho$) for the $NaAlSiO_4$ end member is of the order of +1.5 % at topmost lower mantle pressures and increases to more than +2 % with increasing pressure. For a $Na_{0.7}Mg_{0.3}Al_{1.3}Si_{0.7}O_4$ composition, $\Delta^{S22}\rho$ ranges from +1.2 to +2.0%, whereas for the $MgAl_2O_4$ end member $\Delta^{S22}\rho$ is well below 1 % in the entire pressure range shown. $\Delta^{S22}v_\Phi$, on the other hand, can be as large as −5 % for the $NaAlSiO_4$ end member at topmost lower mantle pressures, although it decreases with increasing pressure. For the $Na_{0.7}Mg_{0.3}Al_{1.3}Si_{0.7}O_4$ composition, $\Delta^{S22}v_\Phi$ is in slightly better agreement at low pressure, but does not improve significantly with increasing pressure due to the smaller $K'_{T0}$ difference between our sample and the model of Stixrude and Lithgow-Bertelloni (2022). The difference becomes smaller than the estimated uncertainty for the CF-type $MgAl_2O_4$ end member. Our findings are of particular interest as $NaAlSiO_4$ and $MgAl_2O_4$ are the two most abundant end-member components in CF-type samples within dry basaltic phase assemblages at lower mantle conditions, with $NaAlSiO_4$ molar fractions oscillating between 50 % and 70 % (Hirose and Fei, 2002; Ishii et al., 2022; Ono et al., 2001). The CF-type phase is expected to comprise 22–26 vol% of a dry basaltic phase assemblage according to most recent phase relations studies (Ishii et al., 2022, Ishii et al., 2019). Based on our calculations, the seismic properties of a dry basaltic assemblage calculated using the EOS parameters for the CF-type phase proposed here will result in $v_\Phi$ and $\rho$ values that are ~1 % lower and ~ 0.3 % higher, respectively, than those calculated using the EOS parameters proposed by Stixrude and Lithgow-Bertelloni (2022). Note that in basaltic systems with 2 wt% $H_2O$ or more, hydrous Al-rich phases, such as $CaCl_2$-type (Al, Fe,Mg,Si)OOH, were reported to form at expense of the CF-type phase (Ishii et al., 2023; Liu et al., 2019). Future phase equilibrium experiments will be needed to assess whether this is also the case for less $H_2O$-rich compositions.

## 5. Conclusion

We determined the isothermal equations of state of three solid solutions of CF-type aluminous silicate phase in the diamond anvil cell by single-crystal synchrotron X-ray diffraction. Structural refinements at high pressure revealed the A-site compressibility, which is determined by the substitution of $Na^+$ by $Mg^{2+}$ and $Fe^{2+}$, to control the bulk compressibility. Specifically, $K_{T0}$ and $K_0^A$ were both found to decrease with decreasing $Na^+$ content. This is in contrast with the elastic parameters proposed by Stixrude and Lithgow-Bertelloni (2022), where $K_{T0}$ slightly increases from the $MgAl_2O_4$ to the $NaAlSiO_4$ end member, which may result in the seismic velocities of subducted basalt at lower mantle conditions to be overestimated. In the FeCF sample, an increase in the compressibility of the unit cell, as well as of the B1 and B2 sites, between approximately 26 and 42 GPa indicates a high-spin to low-spin crossover of $Fe^{3+}$ in octahedral coordination, which may be detectable by seismic methods. Additional experimental work, especially at combined high-pressure and high-temperature conditions, is still needed to constrain the thermoelastic parameters of several CF-type end members. Ultimately, this will help us improve our constraints on the physical properties of basaltic rocks at conditions of the Earth lower mantle.

## CRediT authorship contribution statement

**Giacomo Criniti:** Writing – review & editing, Writing – original draft, Visualization, Methodology, Investigation, Formal analysis, Data curation, Conceptualization. **Tiziana Boffa Ballaran:** Writing – review & editing, Supervision, Methodology, Investigation. **Alexander Kurnosov:** Writing – review & editing, Methodology, Investigation. **Takayuki Ishii:** Writing – review & editing, Methodology, Investigation. **Elena-Marie Rogmann:** Writing – review & editing, Investigation. **Konstantin Glazyrin:** Writing – review & editing, Methodology, Investigation. **Timofey Fedotenko:** Writing – review & editing, Methodology, Investigation. **Daniel J. Frost:** Writing – review & editing, Supervision, Funding acquisition.

## Declaration of competing interest

The authors declare the following financial interests/personal relationships which may be considered as potential competing interests: Giacomo Criniti reports financial support was provided by German Research Foundation. Daniel J. Frost reports financial support was provided by German Research Foundation. Giacomo Criniti reports equipment, drugs, or supplies and travel were provided by German Electron-Synchrotron. Tiziana Boffa Ballaran reports equipment, drugs, or supplies and travel were provided by German Electron-Synchrotron. Alexander Kurnosov reports equipment, drugs, or supplies and travel were provided by German Electron-Synchrotron. Takayuki Ishii reports financial support was provided by Japan Society for the Promotion of Science. If there are other authors, they declare that they have no known competing financial interests or personal relationships that could have appeared to influence the work reported in this paper.

## Data availability

Unit cell data and structural parameters were extracted from the deposited Crystallographic Information Files (CIF).

## Acknowledgments

We thank Raphael Njul for preparing and polishing the samples and Detlef Krauße for his assistance with the electron microprobe analyses. This study was supported by DFG grants FR1555/11 and INST 91/315-1 FUGG. Takayuki Ishii acknowledges support from the Japan Society for the Promotion of Science (JSPS) KAKENHI Grants (Number 23 K19067 and 24 K00735). We acknowledge DESY (Hamburg, Germany), a member of the Helmholtz Association HGF, for the provision of experimental facilities. Parts of this research were carried out at the Extreme Conditions Beamline P02.2, PETRA-III.

## Appendix A. Supplementary data

Supplementary data to this article can be found online at https://doi.org/10.1016/j.pepi.2025.107331.

## References


Akaogi, M., Ishii, T., Yamaura, K., 2024. Post-spinel-type AB2O4 high-pressure phases in geochemistry and materials science. Commun. Chem. 7 (1), 1–12. https://doi.org/10.1038/s42004-024-01278-0.

Angel, R.J., Gonzalez-Platas, J., Alvaro, M., 2014. EosFit7c and a Fortran module (library) for equation of state calculations. Zeitschrift fur Kristallographie 229, 405–419. https://doi.org/10.1515/zkri-2013-1711.

Birch, F., 1947. Finite elastic strain of cubic crystals. Phys. Rev. 71, 809–824. https://doi.org/10.1103/PhysRev.71.809.

Boehler, R., De Hantsetters, K., 2004. New anvil designs in diamond-cells. High Press Res. 24, 391–396. https://doi.org/10.1080/08957950412331323924.

Bruschini, E., Speziale, S., Andreozzi, G.B., Bosi, F., Hålenius, U., 2015. The elasticity of MgAl2O4-MnAl2O4 spinels by Brillouin scattering and an empirical approach for bulk modulus prediction. Am. Mineral. 100, 644–651. https://doi.org/10.2138/am-2015-4993.

Buchen, J., 2021. Seismic wave velocities in Earth's mantle from mineral elasticity. Mantle Convect. Surface Express. 51–95. https://doi.org/10.1002/9781119528609.ch3.

Criniti, G., Ishii, T., Kurnosov, A., Glazyrin, K., Boffa Ballaran, T., 2023. High-pressure phase transition and equation of state of hydrous Al-bearing silica. Am. Mineral. https://doi.org/10.2138/am-2022-8546.

Criniti, G., Boffa Ballaran, T., Kurnosov, A., Liu, Z., Glazyrin, K., Merlini, M., Hanfland, M., Frost, D.J., 2024. Thermal equation of state and structural evolution of Al-bearing bridgmanite. J. Geophys. Res. Solid Earth 129. https://doi.org/10.1029/2023JB026879.

Dubrovinsky, L.S., Dubrovinskaia, N.A., Prokopenko, V.B., Bihan, T.L.E., 2002. Equation of state and crystal structure of NaAlSiO4 with calcium-ferrite type structure in the conditions of the lower mantle. High Press Res. 22, 495–499. https://doi.org/10.1080/08957950212807.

Fei, Y., Ricolleau, A., Frank, M., Mibe, K., Shen, G., Prakapenka, V., 2007. Toward an internally consistent pressure scale. Proc. Natl. Acad. Sci. 104, 9182–9186. https://doi.org/10.1073/pnas.0609013104.

Gonzalez-Platas, J., Alvaro, M., Nestola, F., Angel, R.J., 2016. EosFit7-GUI: a new graphical user interface for equation of state calculations, analyses and teaching. J. Appl. Cryst. 49, 1377–1382. https://doi.org/10.1107/S1600576716008050.

Guignot, N., Andrault, D., 2004. Equations of state of Na-K-Al host phases and implications for MORB density in the lower mantle. Phys. Earth Planet. In. 143, 107–128. https://doi.org/10.1016/j.pepi.2003.09.014.

Hazen, R.M., 1988. A useful fiction: polyhedral modeling of mineral properties. Am. J. Sci. 288-A, 242–269.

Hirose, K., Fei, Y., 2002. Subsolidus and melting phase relations of basaltic composition in the uppermostlower mantle. Geochim. Cosmochim. Acta 66, 2099–2108. https://doi.org/10.1016/S0016-7037(02)00847-5.

Hirose, K., Takafuji, N., Sata, N., Ohishi, Y., 2005. Phase transition and density of subducted MORB crust in the lower mantle. Earth Planet. Sci. Lett. 237, 239–251. https://doi.org/10.1016/j.epsl.2005.06.035.

Hübschle, C.B., Sheldrick, G.M., Dittrich, B., 2011. ShelXle: a Qt graphical user interface for SHELXL. J. Appl. Cryst. 44, 1281–1284. https://doi.org/10.1107/S0021889811043202.

Imada, S., Hirose, K., Komabayashi, T., Suzuki, T., Ohishi, Y., 2012. Compression of Na 0.4Mg 0.6Al 1.6Si 0.4O4 NAL and ca-ferrite-type phases. Phys. Chem. Miner. 39, 525–530. https://doi.org/10.1007/s00269-012-0508-x.

Irifune, T., Ringwood, A.E., Hibberson, W.O., 1994. Subduction of continental crust and terrigenous and pelagic sediments: an experimental study. Earth Planet. Sci. Lett. 126, 351–368. https://doi.org/10.1016/0012-821X(94)90117-1.

Ishii, T., Kojitani, H., Akaogi, M., 2012. High-pressure phase transitions and subduction behavior of continental crust at pressure–temperature conditions up to the upper part of the lower mantle. Earth Planet. Sci. Lett. 357–358, 31–41. https://doi.org/10.1016/J.EPSL.2012.09.019.

Ishii, T., Kojitani, H., Akaogi, M., 2019. Phase relations of Harzburgite and MORB up to the uppermost lower mantle conditions: precise comparison with Pyrolite by multisample cell high-pressure experiments with implication to dynamics of subducted slabs. J. Geophys. Res. Solid Earth 124, 3491–3507. https://doi.org/10.1029/2018JB016749.

Ishii, T., Miyajima, N., Sinmyo, R., Kojitani, H., Mori, D., Inaguma, Y., Akaogi, M., 2020. Discovery of new-structured post-spinel MgFe2O4: crystal structure and high-pressure phase relations. Geophys. Res. Lett. 47, e2020GL087490. https://doi.org/10.1029/2020GL087490.

Ishii, T., Miyajima, N., Criniti, G., Hu, Q., Glazyrin, K., Katsura, T., 2022. High pressure-temperature phase relations of basaltic crust up to mid-mantle conditions. Earth Planet. Sci. Lett. 584, 117472. https://doi.org/10.1016/j.epsl.2022.117472.

Ishii, T., Criniti, G., Wang, X., Glazyrin, K., Ballaran, T.B., 2023. Synthesis and structural analysis of CaFe2O4-type single crystals in the NaAlSiO4-MgAl2O4-Fe3O4 system. Am. Mineral. 108, 217–221. https://doi.org/10.2138/am-2022-8748.

Kaneshima, S., 2019. Seismic scatterers in the lower mantle near subduction zones. Geophys. J. Int. 218, 1873–1891. https://doi.org/10.1093/gji/ggz241.

Kaneshima, S., Helffrich, G., 1999. Dipping low-velocity layer in the mid-lower mantle: evidence for geochemical heterogeneity. Science 1979 (283), 1888–1891. https://doi.org/10.1126/science.283.5409.1888.

Kaneshima, S., Helffrich, G., 2003. Subparallel dipping heterogeneities in the mid-lower mantle. J. Geophys. Res. Solid Earth 108. https://doi.org/10.1029/2001jb001596.

Kantor, I., Prakapenka, V., Kantor, A., Dera, P., Kurnosov, A., Sinogeikin, S., Dubrovinskaia, N., Dubrovinsky, L., 2012. BX90: a new diamond anvil cell design for X-ray diffraction and optical measurements. Rev. Sci. Instrum. 83, 125102. https://doi.org/10.1063/1.4768541.

Kawai, K., Tsuchiya, T., 2010. Ab initio investigation of high-pressure phase relation and elasticity in the NaAlSi2O6 system. Geophys. Res. Lett. 37, n/a–n/a. https://doi.org/10.1029/2010GL044310.

Kawai, K., Tsuchiya, T., 2012. Phase stability and elastic properties of the NAL and CF phases in the NaMg2Al5SiO12 system from first principles. Am. Mineral. 97, 305–314. https://doi.org/10.2138/am.2012.3915.

Klotz, S., Chervin, J.C., Munsch, P., Le Marchand, G., 2009. Hydrostatic limits of 11 pressure transmitting media. J. Phys. D Appl. Phys. 42. https://doi.org/10.1088/0022-3727/42/7/075413.

Kojitani, H., Hisatomi, R., Akaogi, M., 2007. High-pressure phase relations and crystal chemistry of calcium ferrite-type solid solutions in the system MgAl2O4-Mg2SiO4. Am. Mineral. 92, 1112–1118. https://doi.org/10.2138/AM.2007.2255.

Krebs, J.J., Maisch, W.G., 1971. Study of pure and doped cobaltous and nickelous oxide. Phys. Rev. B 4, 750–757. https://doi.org/10.1103/PhysRevB.4.750.

Kurnosov, A., Kantor, I., Boffa-Ballaran, T., Lindhardt, S., Dubrovinsky, L., Kuznetsov, A., Zehnder, B.H., 2008. A novel gas-loading system for mechanically closing of various types of diamond anvil cells. Rev. Scientific Instruments 79, 045110. https://doi.org/10.1063/1.2902506.

Lehmann, G., Harder, H., 1970. Optical spectra of Di-and trivalent Iron in corundum. Am. Mineral. 55, 98–105.

Liermann, H.P., Konôpková, Z., Morgenroth, W., Glazyrin, K., Bednarčik, J., McBride, E. E., Petitgirard, S., Delitz, J.T., Wendt, M., Bican, Y., Ehnes, A., Schwark, I., Rothkirch, A., Tischer, M., Heuer, J., Schulte-Schrepping, H., Kracht, T., Franz, H., 2015. The extreme conditions beamline P02.2 and the extreme conditions science infrastructure at PETRA III. J. Synchrotron Radiat. 22, 908–924. https://doi.org/10.1107/S1600577515005937.

Liu, X., Matsukage, K.N., Nishihara, Y., Suzuki, T., Takahashi, E., 2019. Stability of the hydrous phases of Al-rich phase D and Al-rich phase H in deep subducted oceanic crust. Am. Mineral. 104, 64–72. https://doi.org/10.2138/am-2019-6559.

Mookherjee, M., 2011. Mid-mantle anisotropy: elasticity of aluminous phases in subducted MORB. Geophys. Res. Lett. 38. https://doi.org/10.1029/2011GL047923.

Niu, F., 2014. Distinct compositional thin layers at mid-mantle depths beneath Northeast China revealed by the USArray. Earth Planet. Sci. Lett. 402, 305–312. https://doi.org/10.1016/j.epsl.2013.02.015.

Ohira, I., Jackson, J.M., Solomatova, N.V., Sturhahn, W., Finkelstein, G.J., Kamada, S., Kawazoe, T., Maeda, F., Hirao, N., Nakano, S., Toellner, T.S., Suzuki, A., Ohtani, E., 2019. Compressional behavior and spin state of δ-(Al,Fe)OOH at high pressures. Am. Mineral. 104, 1273–1284. https://doi.org/10.2138/am-2019-6913.

Ono, A., Akaogi, M., Kojitani, H., Yamashita, K., Kobayashi, M., 2009. High-pressure phase relations and thermodynamic properties of hexagonal aluminous phase and calcium-ferrite phase in the systems NaAlSiO4–MgAl2O4 and CaAl2O4–MgAl2O4. Phys. Earth Planet. In. 174, 39–49. https://doi.org/10.1016/J.PEPI.2008.07.028.

Ono, S., Ito, E., Katsura, T., 2001. Mineralogy of subducted basaltic crust (MORB) from 25 to 37 GPa, and chemical heterogeneity of the lower mantle. Earth Planet. Sci. Lett. 190, 57–63. https://doi.org/10.1016/S0012-821X(01)00375-2.

Pamato, M.G., Kurnosov, A., Boffa Ballaran, T., Frost, D.J., Ziberna, L., Giannini, M., Speziale, S., Tkachev, S.N., Zhuravlev, K.K., Prakapenka, V.B., 2016. Single crystal elasticity of majoritic garnets: stagnant slabs and thermal anomalies at the base of the transition zone. Earth Planet. Sci. Lett. 451, 114–124. https://doi.org/10.1016/j.epsl.2016.07.019.

Qin, F., Wu, Y., Xue, S., Zhang, D., Wu, X., Jacobsen, S.D., 2023. Crystal structure of calcium-ferrite type NaAlSiO4 up to 45 GPa. Am. Mineral. 108, 2331–2337. https://doi.org/10.2138/am-2022-8432.

Ricolleau, A., Fei, Y., 2016. Equation of state of the high-pressure Fe3O4 phase and a new structural transition at 70 GPa. Am. Mineral. 101, 719–725. https://doi.org/10.2138/AM-2016-5409/MACHINEREADABLECITATION/RIS.

Ricolleau, A., Perrillat, J.P., Fiquet, G., Daniel, I., Matas, J., Addad, A., Menguy, N., Cardon, H., Mezouar, M., Guignot, N., 2010. Phase relations and equation of state of a natural MORB: implications for the density profile of subducted oceanic crust in the Earth's lower mantle. J. Geophys. Res. Solid Earth 115. https://doi.org/10.1029/2009JB006709.

Rogmann, E.M., Jennings, E.S., Ross, J., Miyajima, N., Walter, M.J., Kohn, S.C., Lord, O. T., 2024. The effect of potassium on aluminous phase stability in the lower mantle. Contrib. Mineral. Petrol. 179, 1–18. https://doi.org/10.1007/S00410-024-02129-W/TABLES/2.

Schollenbruch, K., Woodland, A.B., Frost, D.J., 2010. The stability of hercynite at high pressures and temperatures. Phys. Chem. Miner 37, 137–143. https://doi.org/10.1007/s00269-009-0317-z.

Schollenbruch, K., Woodland, A.B., Frost, D.J., Wang, Y., Sanehira, T., Langenhorst, F., 2011. In situ determination of the spinel–post-spinel transition in Fe3O4 at high pressure and temperature by synchrotron X-ray diffraction. Am. Mineral. 96, 820–827. https://doi.org/10.2138/AM.2011.3642.

Shannon, R.D., 1976. Revised effective ionic radii and systematic studies of interatomic distances in halides and chalcogenides. Acta Crystallogr. A 32, 751–767. https://doi.org/10.1107/S0567739476001551.

Sheldrick, G.M., 2015. Crystal structure refinement with SHELXL. Acta Crystallogr. C Struct. Chem. 71, 3–8. https://doi.org/10.1107/S2053229614024218.

Shen, G., Wang, Y., Dewaele, A., Wu, C., Fratanduono, D.E., Eggert, J., Klotz, S., Dziubek, K.F., Loubeyre, P., Fat'yanov, O.V., Asimow, P.D., Mashimo, T., Wentzcovitch, R.M.M., 2020. Toward an international practical pressure scale: a proposal for an IPPS ruby gauge (IPPS-Ruby2020). High Press Res. 1–16. https://doi.org/10.1080/08957959.2020.1791107.

Stixrude, L., Lithgow-Bertelloni, C., 2011. Thermodynamics of mantle minerals – II. Phase equilibria. Geophys. J. Int. 184, 1180–1213. https://doi.org/10.1111/j.1365-246X.2010.04890.x.

Stixrude, L., Lithgow-Bertelloni, C., 2022. Thermal expansivity, heat capacity and bulk modulus of the mantle. Geophys. J. Int. 228, 1119–1149. https://doi.org/10.1093/GJI/GGAB394.

Strozewski, B., Buchen, J., Sturhahn, W., Ishii, T., Ohira, I., Chariton, S., Lavina, B., Zhao, J., Toellner, T.S., Jackson, J.M., 2023. Equation of state and spin crossover of (Al, Fe)-phase H. J. Geophys. Res. Solid Earth 128, e2022JB026291. https://doi.org/10.1029/2022JB026291.

Sueda, Y., Irifune, T., Sanehira, T., Yagi, T., Nishiyama, N., Kikegawa, T., Funakoshi, K. Ichi, 2009. Thermal equation of state of CaFe2O4-type MgAl2O4. Phys. Earth Planet. In. 174, 78–85. https://doi.org/10.1016/j.pepi.2008.07.046.

Thompson, E.C., Davis, A.H., Brauser, N.M., Liu, Z., Prakapenka, V.B., Campbell, A.J., 2020. Phase transitions in ϵ-FeOOH at high pressure and ambient temperature. Am. Mineral. 105, 1769–1777. https://doi.org/10.2138/am-2020-7468.

Wang, L., Liu, Z., Koizumi, S., Ballaran, T.B., Katsura, T., 2023. Aluminum components in Bridgmanite coexisting with corundum and the CF-phase with temperature. J. Geophys. Res. Solid Earth 128, e2022JB025739. https://doi.org/10.1029/2022JB025739.

Wang, W., Xu, Y., Sun, D., Ni, S., Wentzcovitch, R., Wu, Z., 2020. Velocity and density characteristics of subducted oceanic crust and the origin of lower-mantle heterogeneities. Nat. Commun. 11 (1), 1–8. https://doi.org/10.1038/s41467-019-13720-2.

Wu, Y., Qin, F., Wu, X., Huang, H., McCammon, C.A., Yoshino, T., Zhai, S., Xiao, Y., Prakapenka, V.B., 2017. Spin transition of ferric iron in the calcium-ferrite type aluminous phase. J. Geophys. Res. Solid Earth 122, 5935–5944. https://doi.org/10.1002/2017JB014095.

Yamada, H., Matsui, Y., Ito, E., 1983. Crystal-chemical characterization of NaAlSiO4 with the CaFe2O4 structure. Mineral. Mag. 47, 177–181. https://doi.org/10.1180/minmag.1983.047.343.07.

Yin, K., Zhou, H., Huang, Q., Sun, Y., Xu, S., Lu, X., 2012. First-principles study of high-pressure elasticity of CF- and CT-structure MgAl2O4. Geophys. Res. Lett. 39. https://doi.org/10.1029/2011GL050229.

Zhao, M., Zhou, H., Yin, K., Sun, Y., Liu, X., Xu, S., Lu, X., 2018. Thermoelastic properties of aluminous phases in MORB from first-principle calculation: implications for Earth's lower mantle. J. Geophys. Res. Solid Earth 123, 10583–10596. https://doi.org/10.1029/2018JB016491.